ADVANCED MATERIALS
www.advmat.de

Pseudopolymorphic Phase Engineering for Improved Thermoelectric Performance in Copper Sulfides

Tian-Yu Yang, Shi-Wei Gu, Yi-Xin Zhang, Fengshan Zheng, Deli Kong, Rafal E. Dunin-Borkowski, Di Wu, Zhen-Hua Ge, Jing Feng,* and Lei Jin**

Polymorphism (and its extended form – pseudopolymorphism) in solids is ubiquitous in mineralogy, crystallography, chemistry/biochemistry, materials science, and the pharmaceutical industries. Despite the difficulty of controlling (pseudo-)polymorphism, the realization of specific (pseudo-)polymorphic phases and associated boundary structures is an efficient route to enhance material performance for energy conversion and electromechanical applications. Here, this work applies the pseudopolymorphic phase (PP) concept to a thermoelectric copper sulfide, $Cu_{2-x}S$ ($x \leq 0.25$), via $CuBr_2$ doping. A peak ZT value of 1.25 is obtained at 773 K in $Cu_{1.8}S$ + 3 wt% $CuBr_2$, which is 2.3 times higher than that of a pristine $Cu_{1.8}S$ sample. Atomic-resolution scanning transmission electron microscopy confirms the transformation of pristine $Cu_{1.8}S$ low digenite into PP-engineered high digenite, as well as the formation of (semi-)coherent interfaces between different PPs, which is expected to enhance phonon scattering. The results demonstrate that PP engineering is an effective approach for achieving improved thermoelectric performance in Cu-S compounds. It is also expected to be useful in other materials.

1. Introduction

Polymorphism (and its extended form – pseudopolymorphism) is a common phenomenon in crystals, wherein a solid formed by the same substance crystallizes in different arrangements with (and without) identical chemical composition.[1–4] The constituent phases that are responsible for (pseudo-)polymorphism are referred to as (pseudo-)polymorphs.[1,2,4] They may exhibit different properties (such as density, solubility, electrical, magnetic and mechanical properties, biocompatibility) and are of fundamental importance in mineralogy, crystallography, chemistry/biochemistry, materials science, and the pharmaceutical industries.[5–11] For instance, pyrrhotite (Fe_7S_8), a ferrimagnetic pseudopolymorph of troilite and pyrite, contributes to the magnetization of the continental crust and is used as a magnetic recorder of Earth's history.[12–14]

Control of (pseudo-)polymorphism is difficult, as different (pseudo-)polymorphs are often equivalent energetically, and small changes in crystallization conditions can lead to the formation of different (pseudo-)polymorphic phases.[1,5,8,9,15–17] Despite the difficulty of controlling (pseudo-)polymorphism, the realization of specific (pseudo-)polymorphic phases and the design of associated boundary structures is an important approach for enhancing material performance, in particular for energy conversion and electromechanical applications.[18–21] A striking example is perovskite lead zirconate titanate $PbZr_{1-x}Ti_xO_3$, which exhibits exceptional piezoelectric performance close to its rhombohedral-tetragonal morphotropic phase boundary (MPB) at $x \approx 0.5$.[22–24] Since the rhombohedral and tetragonal phases are structurally similar, the MPB materials are atomically coherent. Piezoelectricity is enhanced due to large polarization rotation and/or polarization extension with MPBs,[18,22,24] and the compositionally induced structural change is maintained under working conditions. Such functional properties of MPB materials can be stable over broad ranges of temperature, time, and pressure.[18]

By taking inspiration from MPB design for electromechanical applications, a similar concept of pseudopolymorphic phase (PP) engineering can be applied to thermoelectric materials. The performance of a thermoelectric material can be evaluated based on the dimensionless figure of merit $ZT = \sigma S^2 T/\kappa$, where σ, S,

T.-Y. Yang, S.-W. Gu, Y.-X. Zhang, Z.-H. Ge, J. Feng
Faculty of Materials Science and Engineering
Kunming University of Science and Technology
Kunming 650093, China
E-mail: z.ge@kust.edu.cn; jingfeng@kust.edu.cn

F. Zheng, D. Kong, R. E. Dunin-Borkowski, L. Jin
Ernst Ruska-Centre for Microscopy and Spectroscopy with Electrons
Forschungszentrum Jülich GmbH
52425 Jülich, Germany
E-mail: l.jin@fz-juelich.de

F. Zheng
Electron Microscopy Center
South China University of Technology
Guangzhou 511442, China

D. Wu
Key Laboratory for Macromolecular Science of Shaanxi Province
Shaanxi Key Laboratory for Advanced Energy Devices
School of Materials Science and Engineering
Shaanxi Normal University
Xi'an 710119, China

The ORCID identification number(s) for the author(s) of this article can be found under https://doi.org/10.1002/adma.202308353

DOI: 10.1002/adma.202308353

T and κ are electrical conductivity, Seebeck coefficient, absolute temperature (in Kelvin) and thermal conductivity, respectively. In the context of ever-growing energy consumption, as well as the threat of environmental pollution, the thermoelectric technique has been used since the last century as a potential clean energy source for thermoelectricity-related conversion scenarios.[25–30] As proposed by Slack, a thermoelectric material is a "phonon-glass electron-crystal" (PGEC).[31] It is usually a superior resistor of heat (i.e., a phonon glass) and a good conductor of electricity (i.e., an electron crystal). The ability to efficiently convert heat to electricity and vice versa forms the basis of thermoelectric technology.

Here, we study copper sulfides ($Cu_{2-x}S$, $x \leq 0.25$), a promising thermoelectric system with complex phase structures, as a model system for introducing PP engineering (PPE) to enhance thermoelectric performance. In combination with atomic-resolution scanning transmission electron microscopy (STEM), we demonstrate effective PPE via $CuBr_2$ doping. In this system, the PP phase consists primarily of a cubic-like superstructure phase and a hexagonal (h) phase. We find that high thermoelectric performance can be achieved by converting the matrix from the pristine $Cu_{1.8}S$ low digenite phase to the PP-engineered high digenite phase. The formation of (semi-)coherent interfaces between the different PPs, as revealed by atomic-resolution STEM, is thought to enhance phonon scattering. At 773 K, $Cu_{1.8}S$ + 3 wt% $CuBr_2$ exhibits a peak ZT value of 1.25, which is twice that of a pristine sample.

2. PPE of Copper Sulfides

We begin with a brief description of the phase structures of copper sulfides. Copper sulfides ($Cu_{2-x}S$) are generally categorized into three groups based on their chemical compositions: digenite ($x \approx 0.2$), djurleite ($x \approx 0.06$) and chalcocite ($x = 0$).[32] Digenite is regarded as a potential thermoelectric material in the medium temperature range due to its ultrahigh electrical conductivity and relatively stable electrical transport properties.[33,34] In particular, $Cu_{1.8}S$ digenite (also written $Cu_{7.2}S_4$ or Cu_9S_5), i.e., *high* digenite, stabilizes in a cubic antifluorite structure (space group Fm-3m; $a \approx 5.6$ Å) with ≈10 at% Cu vacancies at temperatures above 346–361 K.[32,35–39] As a result of the presence of Cu vacancies, the digenite phase exhibits p-type conduction. Upon cooling across ≈350 K, this cubic high digenite, which is referred to as the 1a phase based on the nomenclature given,[40] transitions to the *low* digenite phase, which remains stable below room temperature (RT).[35,38,40,41] This transition can be recognized by the appearance of satellite reflections along the $<111>_{1a}$ body diagonal in a diffraction pattern viewed along $<1\bar{1}0>_{1a}$.[35,37,40–42] As the high and low digenite phases are compositionally identical, this temperature-controlled transition is a reversible polymorphic phase transition.

The crystal structure of the low digenite phase has remained elusive. Early precession X-ray diffraction (XRD) studies suggested a rhombohedral (r) structure (space group R-3m; a_r = 16.16 Å, α_r = 13°56′) constructed from the cubic 1a phase via twinning mediation.[35,42,43] Subsequent real space high-resolution transmission electron microscopy studies revealed that the low digenite phase is most likely a chemically modulated superstructure of the 1a phase as a result of Cu vacancy ordering, as illustrated schematically in **Figure 1a**. This ordered phase is termed *Na* (i.e., an abbreviated form of *NaNaNa*), where N is found to be 4–6 (depending on the modulated periodicity of the cubic sub-cell a).[40,41] As a consequence of Cu chemical ordering, the *Na* superstructure can be divided into two subregions: a Cu-rich region (CRR) and a vacancy-rich region (VRR). In comparison with the CRR, the stoichiometric ratio of Cu atoms decreases in the VRR, resulting in a compositional difference with a relatively higher valence state of Cu (i.e., Cu^{2+}) (Figure 1a).

Although the intrinsically high vacancy nature of the low digenite $Cu_{1.8}S$ phase results in ultrahigh electrical conductivity, it is detrimental to thermoelectric performance because of the positive correlation between electrical conductivity and thermal conductivity. The fact that the presence of Cu superionicity[33] accompanied by Cu chemical disorder in the high digenite phase can greatly reduce thermal conductivity and lead to better thermoelectric properties provides a motivation to study the stabilization of this high temperature (HT) cubic phase as a RT matrix/host material. Accordingly, here we apply PPE to pristine $Cu_{1.8}S$ via Cu^{2+} doping.

As a consequence of the presence of compositional differences in the pristine *Na* phase (Figure 1a), the additional Cu dopant is hypothesized to preferentially fill VRRs (by occupying vacant Cu sites), leading to an assimilated Cu distribution in the entire *Na* phase. The elimination of compositional differences between the CRRs and VRRs facilitates the formation of the cubic 1a phase. As Cu^{2+} is a Jahn-Teller active ion[44,45] from a valence perspective, a further increase of Cu^{2+} at local VRRs may result in an energy instability, stimulating a transformation from the *Na* phase to the 1a phase (Figure 1b). In contrast to a temperature-induced polymorphic phase transition, such an *Na* to 1a transformation is pseudopolymorphic and considered to be irreversible.

As the ultrahigh electrical conductivity of pure $Cu_{1.8}S$, which is associated with the presence of intrinsic hole carriers, is detrimental to the thermal properties of digenite, we chose to substitute Br^- for S^{2-} anions to compensate for holes, such that both Br^- and Cu^{2+} can introduce electrons to reduce the carrier concentration and lower the carrier-related thermal conductivity.

On further increasing the Cu^{2+} doping level, other PPs such as djurleite and/or chalcocite,[46–48] are expected to form in the cubic matrix, as shown in Figure 1c. Their coexistence may result in the formation of (semi-)coherent phase boundaries. The presence of a mixed-phase structure and (semi-)coherent phase boundaries can scatter phonons and lower the lattice thermal conductivity (Figure 1d).

3. Results and Discussion

3.1. Phase Structures

Figure 2a,b shows XRD results recorded from bulk $Cu_{1.8}S$ + x wt% $CuBr_2$ (x = 0, 1, 2, 3, 5) specimens. Pristine $Cu_{1.8}S$ exhibits extra reflections (e.g., at $2\theta \approx 30°$; see the vertical arrow) in addition to the cubic peaks, as a result of the presence of structural modulations, as previously reported for the RT low digenite phase.[35,42] Here, we use JCPDS #23-0962, which is a rhombohedral crystal structure, as a reference. This observation does not rule out the possible presence of the *Na* modulated structure, as discussed in Section 2. The extra reflections disappear as the

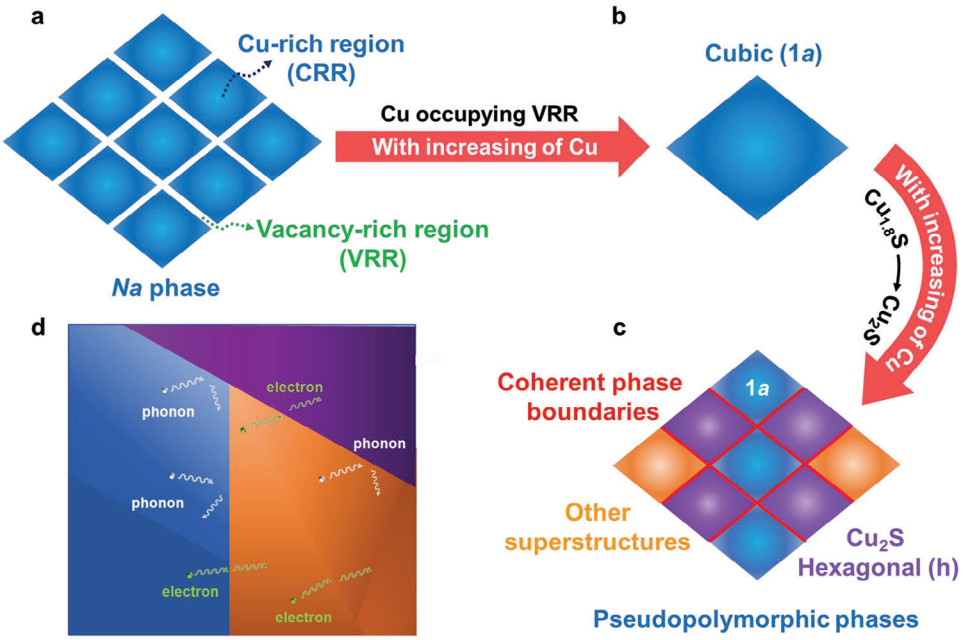

Figure 1. Schematic diagrams of a polymorphic phase structure and its performance correlation. a) The room-temperature-stable *Na* phase of $Cu_{1.8}S$, formed as a result of Cu vacancy ordering. (See text for details). Blue areas are Cu-rich regions (CRRs), while the areas in between are Cu vacancy-rich regions (VRRs). b) Upon the addition of $CuBr_2$, the original chemical ordering may be disrupted. The introduced Cu ions are thought to occupy the VRRs, triggering a transformation from *Na* to the chemically disordered 1*a* phase. c) Upon further introduction of $CuBr_2$, other phases, such as high-Cu-content djurleite and/or chalcocite, may form in the cubic 1*a* matrix, leading to the coexistence of pseudopolymorphic phases (PPs) and the formation of coherent phase boundaries/interfaces. d) Schematic diagram the formation of multiphase interfaces, which selectively scatter carriers and strongly scatter phonons. The PP structure and coherent interfaces have a small effect on electron scattering, but can strongly scatter phonons, thereby enhancing thermoelectric properties.

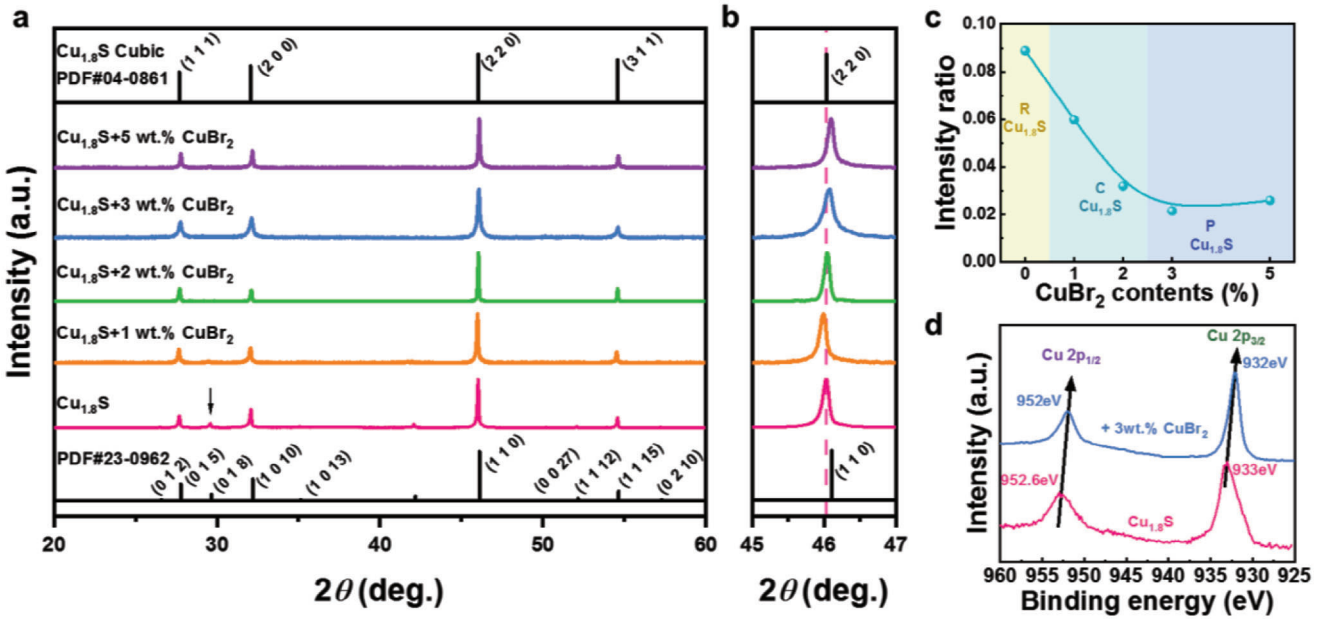

Figure 2. a) X-ray diffraction (XRD) patterns recorded from bulk $Cu_{1.8}S + x$ wt% $CuBr_2$ ($x = 0, 1, 2, 3, 5$) samples. b) Magnified XRD pattern for 2θ values between 45° and 47°. c) Ratio of peak intensity between $(018)_r$ and the strongest $(110)_r$ or $(220)_{1a}$ reflections plotted as a function of $CuBr_2$ doping concentration. d) X-ray photoelectron spectra recorded from $Cu_{1.8}S$ and $Cu_{1.8}S + 3$ wt% $CuBr_2$ showing Cu $2p_{1/2}$ and Cu $2p_{3/2}$ peak shifts toward the low binding energy direction, suggesting a decrease in Cu valence upon Cu^{2+} incorporation.

doping level increases, suggesting that a structural transition occurs to the cubic high digenite 1*a* phase (JCPDS #04-0861). No impurity phase was detected using XRD in any sample. Electron probe X-ray micro-area analysis confirms the XRD results, providing a Cu to S atom ratio in $Cu_{1.8}S$ + 3 wt% $CuBr_2$ of ≈1.8, as shown in Figures S1 and S2 (Supporting Information).

Fading of peaks in the XRD pattern is associated with a progressive transition from the RT low digenite phase to the high digenite cubic phase. Figure 2c shows this evolution more clearly, in the form of a plot of intensity ratio between the fading $(018)_r$ peak at $2\theta \approx 30°$ and the strongest $(110)_r$ or $(220)_{1a}$ peak. A PP transition occurs at a $CuBr_2$ doping level of between 0 and 2 wt%. Figure 2b shows a magnified XRD pattern, in which the $2\theta \approx 46°$ peak shows a turning point (TP) at $x = 1$. Figure 2d shows X-ray photoelectron spectroscopy (XPS) results, which reveal that the Cu $2p_{1/2}$ and Cu $2p_{3/2}$ peaks shift toward the low binding energy direction, indicating a decrease in Cu valence upon Cu^{2+} incorporation. The decrease in Cu valence also suggests that Cu^{2+} undergoes a reduction reaction.

These results show that $CuBr_2$ provides an effective means to tune the phase structure of $Cu_{1.8}S$ and suggest that PPE can be an alternative way to modulate the phase structure in the Cu-S system using Cu^{2+} ions. The phase transition is driven by changes in chemical composition rather than temperature, indicating that PPE provides a stable and robust approach.

3.2. Atomic-Scale Observations of PPs in $Cu_{1.8}S$

Figure 3 shows a high-angle annular dark-field (HAADF) STEM image and corresponding fast Fourier transform (FFT) images recorded from pristine (Figure 3a–c) and 3 wt% $CuBr_2$ doped (Figure 3d–h) $Cu_{1.8}S$. For pristine $Cu_{1.8}S$ (Figure 3a), the relatively homogenous contrast suggests high phase purity. Figure 3b shows an atomic-scale HAADF–STEM image that confirms the formation of an *Na* superstructure in the pristine sample. Here $N = 6$, as determined from the corresponding FFT image in Figure 3c. This finding is consistent with the XRD result (Figure 2a). Since HAADF–STEM image contrast is approximately proportional to Z^2 (where Z is atomic number), the chessboard-like intensity modulation in Figure 3b reflects the distribution of Cu chemical ordering. These observations are consistent with the schematic diagrams in Figure 1a.

In contrast, Figure 3d,e shows low-magnification and medium-magnification HAADF–STEM images of the 3 wt% $CuBr_2$ doped sample, respectively. The uneven contrast suggests a mixed phase configuration in each grain. Three phases are found in the 3 wt% $CuBr_2$ doped sample (Figure 3f–k). First, the progression from Figure 3c–f suggests that the matrix structure in the doped sample transformed from the 6*a* phase to a cubic 1*a* phase. All of the 6*a* satellite spots have disappeared in Figure 3f. Figure 3i shows that the ordering-related chessboard-like feature (Figure 3b) has been replaced by a homogenous fully disordered atomic pattern. These observations are consistent with the formation of the cubic 1*a* phase at RT.

In addition to the 1*a* phase of the matrix, a superstructure phase (see bright areas in Figure 3e) and a h phase are observed. Corresponding FFT images are shown in Figure 3g,h, respectively. Within the h phase, there is also an intergrown monoclinic (m) phase that shows full lattice coherence to the h phase, as shown in Figure S3 (Supporting Information). No compositional difference was detected between the three phases in the investigated areas using energy dispersive X-ray spectroscopy (EDXS), suggesting the absence of significant Br segregation.

An in-depth examination of the superstructure phase in Figure 3g shows that the marked spots (circles) are coherent with the cubic phase (Figure 3f), suggesting that this is a superstructure form of the 1*a* phase. A comparison of Figure 3f,g indicates that the superstructure phase is 1*a*1*a*2*a* (i.e., $a_{1a1a2a} = b_{1a1a2a} = a$, $c_{1a1a2a} = 2a$), with the atomic arrangement shown in Figure 3j. A similar superstructure (with an unknown atomic structure) was observed in the bornite-digenite system, possibly as a result of electron beam irradiation of the 1*a* substructure.[40] The present 1*a*1*a*2*a* superstructure phase is stable in the presence of electron beam irradiation and is therefore likely to have formed during synthesis.

The h phase (Figure 3h) has an orientation relationship with the cubic matrix of $[\bar{2}110]_h \parallel [1\bar{1}0]_{1a}$ and $(0002)_h \parallel (111)_{1a}$ (marked by a yellow circle), which is commonly observed in cubic-hexagonal coexisting systems. The h phase is considered to have a high chalcocite Cu_2S structure[46–48] based on electrical conductivity measurements (see below). The atomic-scale HAADF–STEM image shown in Figure 3k matches a simulation for Cu_2S based on an ICSD-43323 model. Direct proof using compositional measurement techniques such as EDXS is challenging, as variations in Cu concentration between different PPs are subtle (the atomic percentages are between 63.6% and 66.7% across the entire $Cu_{2-x}S$, $x \leq 0.25$ group).

The boundary/interface regions between the observed phases are investigated further in **Figure 4** using atomic-scale HAADF–STEM. Figure 4a shows a coherent interface between the cubic 1*a* and superstructure 1*a*1*a*2*a* phases, as confirmed in the FFT patterns shown in Figure 3f,g. Figure 4b shows a coherent boundary between the cubic 1*a* matrix and the hexagonal Cu_2S phase. As a result of the presence of two equivalent $<111>_{1a}$ directions in the cubic phase, i.e., $[\bar{1}\bar{1}1]_{1a}$ and $[111]_{1a}$, the h phase can form two structural domains, i.e., h-1 and h-2, with $[0001]_{h\text{-}1} \parallel [\bar{1}\bar{1}1]_{1a}$ and $[0001]_{h\text{-}2} \parallel [111]_{1a}$, respectively. The hexagonal domains can form cubic-{111}-twinning-like boundaries (see Figure 4c and inset) with angles of ≈70°. The formation of PPs and associated coherent and twinning-like boundaries is believed to play a significant role in the enhancement of phonon scattering.

Furthermore, our in situ XRD and STEM results (Figures S4 and S5, Supporting Information) reveal that the matrix 1*a* and h phases and their associated interfaces are maintained up to at least ≈770 K (limited by the heating instrument in our microscope) and that there is no 1*a* to 6*a* return transtion. Such phase robustness is critically important for PPE.

3.3. Thermoelectric Properties

Figure 5 shows the thermoelectric properties of the $Cu_{1.8}S + x$ wt% $CuBr_2$ specimens. The electrical conductivity of each sample (Figure 5a) exhibits a roller-coaster-like trend, first increasing and then decreasing as the temperature increases, suggesting that the conductivity changes from semiconducting (before the TP) to metallic (after the TP).

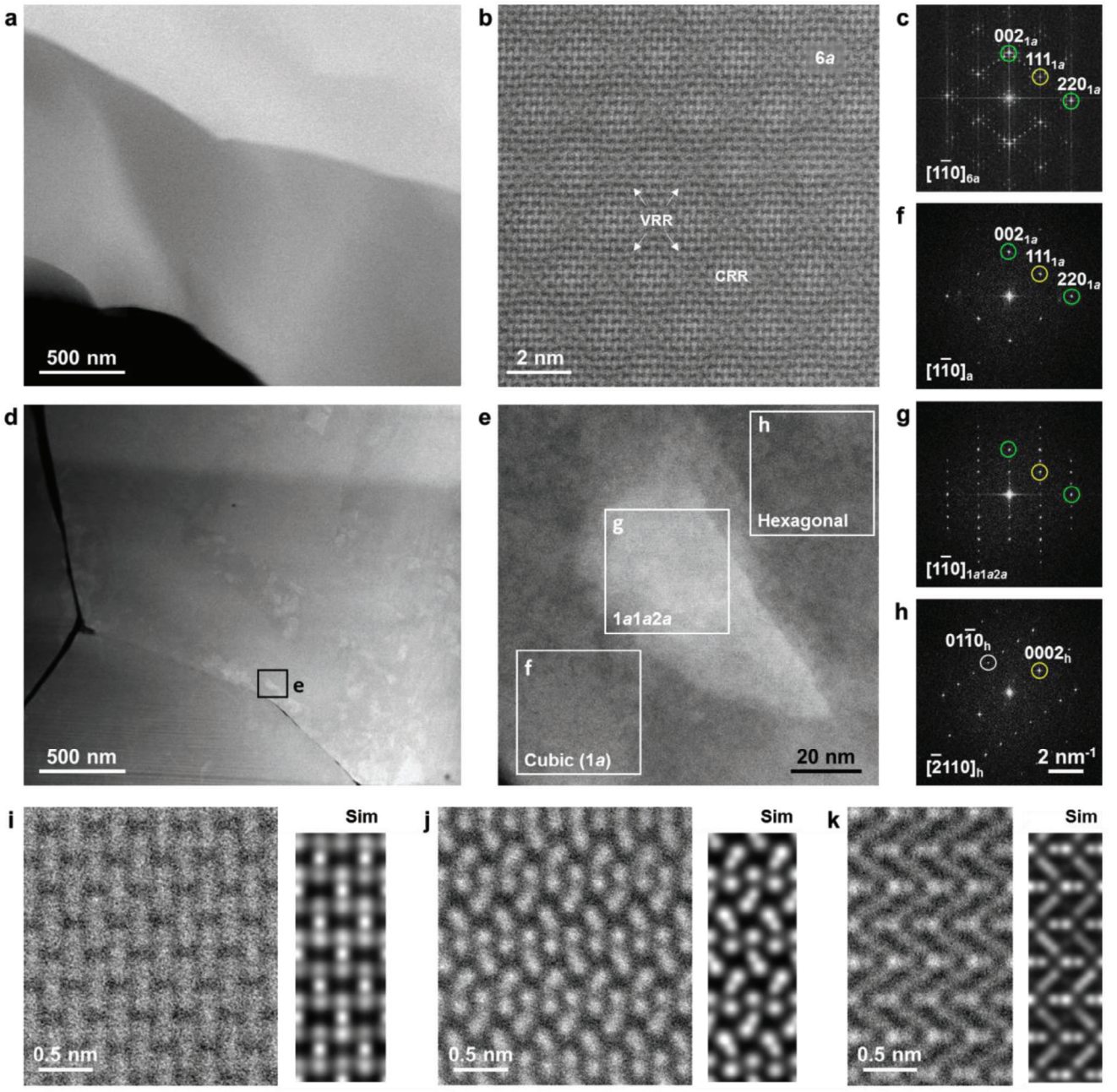

Figure 3. Scanning transmission electron microscopy (STEM) of $Cu_{1.8}S$ + 3 wt% $CuBr_2$. a) Low-magnification high-angle annular dark-field (HAADF) STEM image of pristine $Cu_{1.8}S$. b) Atomic-resolution HAADF–STEM image of the chessboard-like pristine sample. c) Corresponding fast Fourier transform (FFT) image. d) Low-magnification and e) medium-magnification HAADF–STEM images of 3 wt% $CuBr_2$ doped $Cu_{1.8}S$. Three phase structures are observed. f–h) Corresponding FFT images of the three phase structures marked in e. i–k) Atomic-resolution HAADF–STEM images and corresponding simulations of the 1*a*, 1*a*1*a*2*a* and h phases, respectively.

Since the TP reflects the temperature-driven polymorphic phase transition in $Cu_{2-x}S$ directly, it can be used to understand the phase configurations. Figure 5a shows that the TP of the pristine sample occurs at 361 K, which is consistent with the transition of $Cu_{1.8}S$ between the low and high digenite phases.[32,35–39] In contrast, there is no such TP in the 1 and 2 wt% samples, suggesting the formation of the cubic phase at RT. This observation is in agreement with the XRD result shown in Figure 1a. The phase transition temperatures of the 3 and 5 wt% $CuBr_2$ doped samples increase to ≈425 K, suggesting the presence of $Cu_{1.96}S$ or Cu_2S phases.[46–48] However, these phases were not detected using XRD, probably because their amount is limited and/or their structural symmetry is relatively low (when compared with the cubic phase). Our STEM results in Figures S3 and S5 (Supporting Information) show that this transition corresponds to the m to h phase transition of Cu_2S.

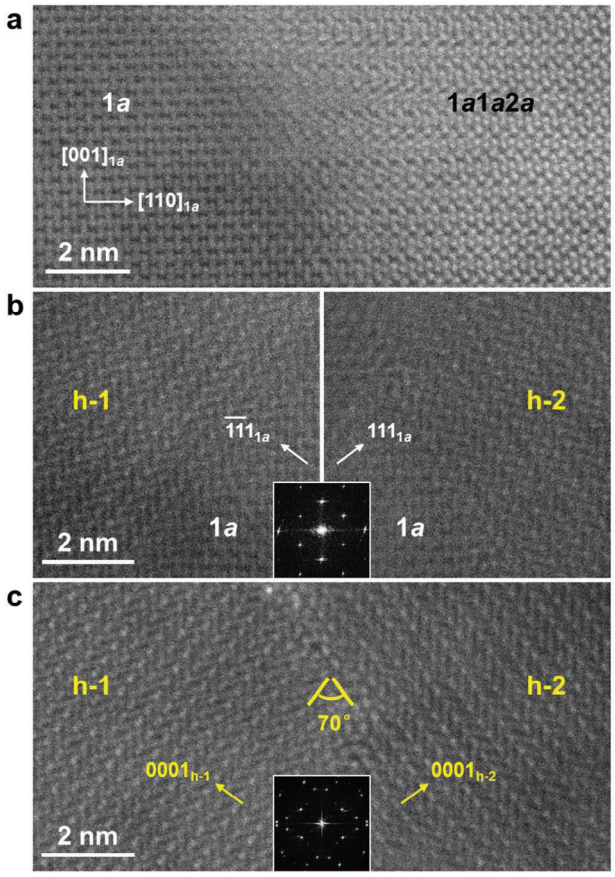

Figure 4. Atomic-resolution high-angle annular dark-field scanning transmission electron microscopy images of interface structures. a) Fully coherent interface between the 1*a* and superstructure 1*a*1*a*2*a* phases. b) Coherent phase boundary between the hexagonal (h) Cu_2S phase and the cubic 1*a* matrix. c) Twinning-like boundary formed by two hexagonal domains.

The electrical conductivity decreases as the doping level is increased, primarily due to a change in the concentration and mobility of electrical carriers, as evidenced by RT Hall measurements. (See Figure S6, Supporting Information). This reduction may be attributed to the introduction of Cu^{2+} to Cu vacancy sites, as well as to the substitution of S^{2-} by Br^- in the matrix phase, both of which introduce additional electrons. In order to maintain electroneutrality, holes in the *p*-type matrix are expected to annihilate with the introduced electrons, reducing the carrier concentration *n*. The presence of pores in the doped sample (see Figure S7, Supporting Information) may also reduce the carrier mobility.

Figure 5b shows the temperature dependence of the Seebeck coefficient for the $Cu_{1.8}S + x$ wt% $CuBr_2$ samples. Each sample shows a positive *S*, confirming its *p*-type semiconducting nature. *S* increases gradually due to a decrease in *n*, as well as likely an enhancement in scattering from PP interfaces, especially for the 5 wt% doped sample, in which the highest value of *S* is 130 μV K^{-1} at 773 K.

As *S* is related to electronic effective mass *m**, a Pisarenko relationship (where the Pisarenko curve describes the relationship between *n* and *S*) based on a single parabolic band model was determined from the measured RT Seebeck coefficient plotted as a function of *n*. Figure 5c shows that the effective masses of the 1 and 2 wt% $CuBr_2$ doped samples remain relatively stable ($m^* = 0.6\ m_0$, where m_0 is the mass of a stationary electron). In contrast, *m** increases to ≈0.8 m_0 upon the addition of 3 and 5 wt% $CuBr_2$, respectively. The introduction of Cu may optimize the energy density of states, resulting in an enhancement of *m**. The *S*-*n* relationship for degenerate semiconductors and metals can be described in the form $S = \frac{8\pi^2 k_B^2}{3eh^2} m^* T\left(\frac{\pi}{3n}\right)^{2/3}$, where k_B and *h* are the Boltzmann constant and Planck constant, respectively.[49] A decrease in *n* and an increase in *m** both optimize *S*.

Although *S* is improved in each sample, the power factor ($PF = \sigma S^2$) is lower in the doped samples than the pristine sample. Figure 5d shows that the *PF* of the $Cu_{1.8}S$ + 3 wt% $CuBr_2$ sample is 1288 μW m^{-1} K^{-2} at 773 K, which is lower than the value of 1310 μW m^{-1} K^{-2} in the pristine specimen.

Figure 5e shows that the decrease in electrical properties is accompanied by a decrease in thermal conductivity. Between all of the samples, $Cu_{1.8}S$ + 5 wt% $CuBr_2$ has the lowest value of κ of 0.72 W m^{-1} K^{-1} at 773 K, which is well below that of the pristine $Cu_{1.8}S$ sample. This decrease in κcan be interpreted as follows. First, scattering of phonons from PP structures and (semi-)coherent phase boundaries reduces the lattice thermal conductivity (κ_l). Second, electrons introduced by $CuBr_2$ doping compensate for holes in the $Cu_{1.8}S$ matrix, reducing the overall *n*and lowering σ. This reduction in σ can affect the contribution of carrier thermal conductivity (κ_e) to the total thermal conductivity ($\kappa = \kappa_l + \kappa_e$). Third, point defects introduced by ion substitution can scatter high frequency phonons, while pores created at grain boundaries may be responsible for scattering low frequency phonons.

Figure 5f shows that, as a result of its intrinsically low *S*and high κ, the ZT value of pristine $Cu_{1.8}S$ is only 0.54 at 773 K. Doping with $CuBr_2$ enhances ZT in each sample significantly. At 773 K, the $Cu_{1.8}S$ + 3 wt% $CuBr_2$ bulk sample exhibits the highest ZT value of 1.25, which is 2.3 times higher than that of undoped $Cu_{1.8}S$, showing that $CuBr_2$ is an effective dopant for improving the thermoelectric properties of $Cu_{1.8}S$.

In order to better evaluate the influence of PPE on thermoelectric performance, the ratio of the σ inflection point value (i.e., σ_0) to its previous value (based on Figure 5a) was used as a measure of the strength of the phase transition upon heating. The result is shown in **Figure 6a**. The pristine sample has the highest ratio, resulting from the 6*a* to 1*a* phase transition reported in the literature. As the introduction of $CuBr_2$ stabilizes the 1*a* PP at RT, there is no strong phase transition upon heating, leading to a large decrease in the ratio for the 1 and 2 wt% doped samples. A further increase in $CuBr_2$ results in an increase in the ratio due to the formation of the Cu_2S phase. However, it is still lower than that for the pristine case. It should be noted that the temperature-induced phase transition may result in a volume change, which can cause device failure in real applications. The PPE concept can suppress/remove such temperature-driven transitions. Figure 6b shows thermal conductivity plotted as a function of $CuBr_2$ doping content. The lattice thermal conductivity (Figure S8, Supporting Information) was calculated for each sample by using a modified equation of the form $\kappa_l = L\sigma T$, where *L* is the Lorentz constant determined to be 0.7 for Cu-S based superionic

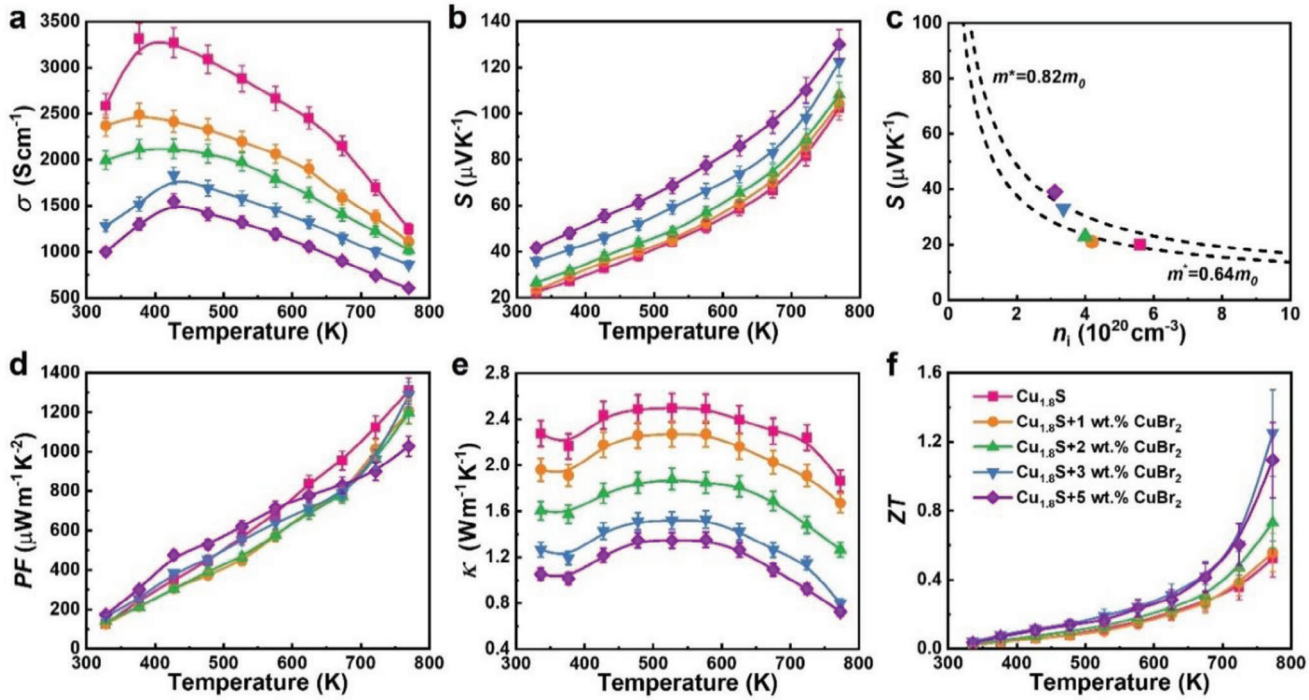

Figure 5. Temperature-dependent thermoelectric properties of $Cu_{1.8}S$ + *x* wt% $CuBr_2$ (*x* = 0, 1, 2, 3, 5). a) Electrical conductivity σ and b) Seebeck coefficient *S* plotted as a function of measured temperature *T*. c) Room temperature correlation between *S* and carrier concentration *n* for the $Cu_{1.8}S$ + *x* wt% $CuBr_2$ (*x* = 0, 1, 2, 3, 5) samples, fitted using Pisarenko curves based on a single parabolic band model. d) Power factor $PF = \sigma S^2$. e) Thermal conductivity κ and f) thermoelectric figure of merit ZT plotted as a function of *T*.

conductors. Details of the calculation are given in the Supporting Information.[33,48] κ_l decreases as the material transforms into the cubic phase. On further increasing the dopant content, the PP structure forms and κ_l is effectively optimized. In this way, the PP structure optimizes κ_l and weakens electron-phonon scattering in thermal transport. The Debye–Callaway model[50] prediction (Figure S9, Supporting Information) indicates that phase boundaries introduced by PPE are mainly responsible for scattering low-frequency phonons. Figure 6c shows ZT and κ at 773 K for the samples doped with $CuBr_2$. Upon the development of PPs and the formation of (semi-)coherent interfaces, κ is effectively reduced and the thermoelectric performance is greatly improved.

4. Conclusion

In this paper, PPE has been realized in $Cu_{1.8}S$ via Cu^{2+} doping for thermoelectric applications. The introduction of $CuBr_2$ into the matrix is found to enhance the Seebeck coefficient and to reduce thermal conductivity. PPE achieves these results through carrier concentration regulation and structural modulation. At 773 K, the highest ZT value of 1.25 obtained for a $Cu_{1.8}S$ + 3 wt% $CuBr_2$ sample is 2.3 times higher than that of a pristine sample. These results provide the first report of the stable synthesis of cubic phase $Cu_{1.8}S$ thermoelectric material at RT, as well as the orientation relationships between the PPs. They provide suggestions for enhancing crystal structure stability in the copper sulfide system and a reference concept for optimizing the structures of other (pseudo-)polymorphic thermoelectric materials, such as SnSe, Cu_2Se, GeTe, and $Cu_{12}Sb_4S_{13}$. Stabilization of the HT phase at RT for thermoelectric materials may also remove the phase transition point during the heating process, thereby avoiding a volume change that may cause device failure.

5. Experimental Section

Material Synthesis: The studied $Cu_{1.8}S$ samples were obtained from stoichiometrically weighed Cu (99.99%, <200 mesh) and S (99.99%, <200 mesh) raw materials. The resulting $Cu_{1.8}S$ and *x* wt% $CuBr_2$ (*x* = 0, 1, 2, 3, 5, powder, 99.99%, <200 mesh) were mixed, vacuum sealed in quartz glass tubes (pressure below 5×10^{-4} Pa), and reacted based on the solid-state reaction method in a vertical pit furnace. The furnace was heated from RT to 673 K over 6 h, kept at 673 K for 6 h, heated to 1273 K over 6 h, kept at 1273 K for 6 h, and was cooled to RT over 6 h. The resulting ingots were ground for 10 min in a protective atmosphere (95 vol% Ar + 5 vol% H_2) using high energy ball milling at 800 rpm to produce a fine powder. The powder was placed in a graphite mold with a size of Φ20 mm, vacuumed to below 4 Pa in a spark plasma sintering furnace and sintered at 773 K for 5 min at a pressure of 50 MPa to obtain the dense bulk. The sintered bulk was cut and ground into long strips or disks for different measurements.

Sample Characterization: The phase structure of the bulk samples was characterized by using XRD (MiniFlex600 Rigaku, Japan) with Cu K_α radiation (λ = 1.54 Å). Valence states in the $CuBr_2$ doped $Cu_{1.8}S$ sample were characterized using XPS. The fracture morphology of the sample was studied using field emission scanning electron microscopy and its atomic structure was revealed using aberration-corrected STEM (FEI Titan G^2 80–200 ChemiSTEM equipped with a super-X EDXS system, operated at 200 kV). Electron microscopy image simulations were performed using Dr. Probe software[51] for the experimental illumination parameters (convergence semi-angle 25 mrad and collection semi-angle 70–200 mrad). The carrier concentration and carrier mobility of the sample at RT were

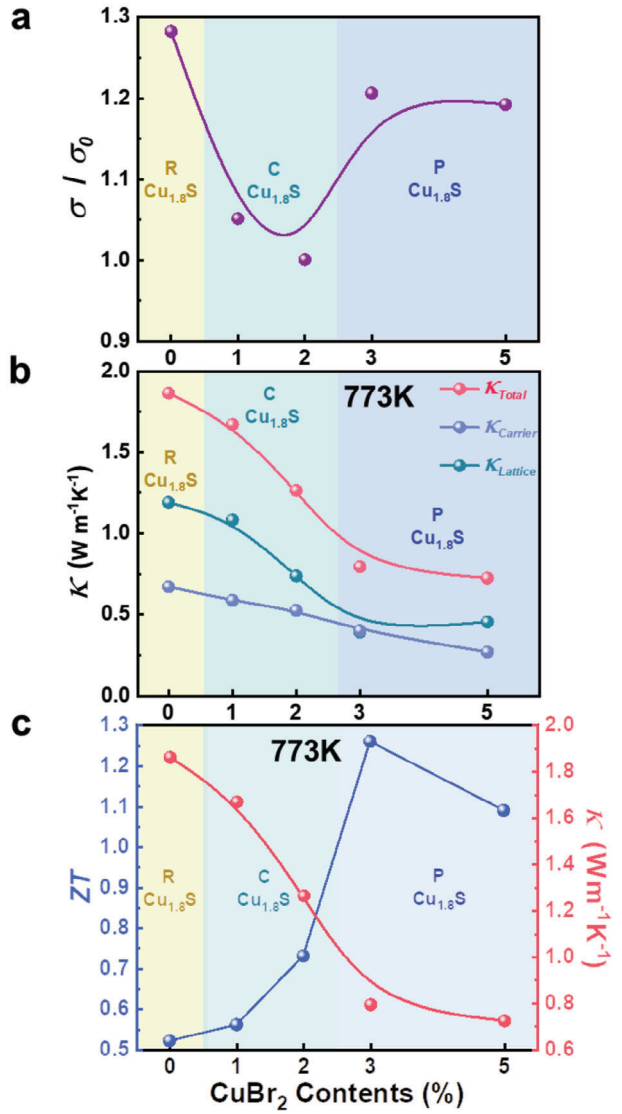

Figure 6. Relationship between $CuBr_2$ content variation and the structural and thermoelectric properties of $Cu_{1.8}S$. a) Ratio of the conductivity inflection point to its previous point plotted as a function of doping content. b) Effect of pseudopolymorphic phase (PP) structures on thermal conductivity caused by $CuBr_2$ content variation. c) Relationship between PP structures and thermoelectric properties.

measured by using a Hall effect measurement system. Electrical and thermal properties of the samples were obtained by using a Seebeck coefficient measurement system (ZEM-3, ULVAC, Japan) and a laser thermal conductivity meter (NETZSCH LFA-467, Germany), respectively. For the parameters required for the thermal performance calculation, the heat capacity (C_p) was obtained from a synchronous thermal analyzer (NETZSCH STA-449, Germany) and the density (ρ) from the Archimedes method. Errors associated with the measurements of σ, S, C_p and ρ were approximately 3–4%, while the range of the ZT error bars was approximately 15–20%.

Supporting Information

Supporting Information is available from the Wiley Online Library or from the author.

Acknowledgements

This work was supported by the National Natural Science Foundation of China (Grant No. 52162029), the Yunnan Provincial Natural Science Key Fund (Grant No. 202101AS070015), the National Key R&D Program of China (No. 2022YFF0503804), and the Outstanding Youth Fund of Yunnan Province (Grant No. 202201AV070005). L.J. is grateful for support from a Feodor Lynen Research Fellowship from the Alexander von Humboldt Foundation during the stay in Weizmann Institute of Science, Israel. T.T.Y. and W.S. are acknowledged for their assistance with STEM sample preparation.

Open access funding enabled and organized by Projekt DEAL.

Conflict of Interest

The authors declare no conflict of interest.

Data Availability Statement

The data that support the findings of this study are available from the corresponding author upon reasonable request.

Keywords

atomic-resolution scanning transmission electron microscopy, copper sulfide, (pseudo-)polymorphic phase engineering, thermoelectric materials

Received: August 17, 2023
Revised: October 26, 2023
Published online: December 7, 2023

[1] B. K. Saha, N. K. Nath, R. Thakuria, *Chem. Rec.* **2023**, *23*, 202200173.
[2] B. Bechtloff, S. Nordhoff, J. Ulrich, *Cryst. Res. Technol.* **2001**, *36*, 1315.
[3] A. Nangia, G. R. Desiraju, *Chem. Commun.* **1999**, 605.
[4] A. Nangia, *Cryst. Growth Des.* **2006**, *6*, 2.
[5] H. Bergeron, D. Lebedev, M. C. Hersam, *Chem. Rev.* **2021**, *121*, 2713.
[6] A. M. Bragança, A. Minoia, R. Steeno, J. Seibel, B. E. Hirsch, L. Verstraete, O. Ivasenko, K. Müllen, K. S. Mali, R. Lazzaroni, S. De Feyter, *J. Am. Chem. Soc.* **2021**, *143*, 11080.
[7] Y. A. Eshete, K. Kang, S. Kang, Y. Kim, P. L. Nguyen, D.-Y. Cho, Y. Kim, J. Lee, S. Cho, H. Yang, *Adv. Mater.* **2022**, *34*, 2202633.
[8] D. Gentili, M. Gazzano, M. Melucci, D. Jones, M. Cavallini, *Chem. Soc. Rev.* **2019**, *48*, 2502.
[9] J. Mei, J. Wang, H. Gu, Y. Du, H. Wang, Y. Yamauchi, T. Liao, Z. Sun, Z. Yin, *Adv. Mater.* **2021**, *33*, 2004920.
[10] F. Zhang, Y. Wu, H. Lou, Z. Zeng, V. B. Prakapenka, E. Greenberg, Y. Ren, J. Yan, J. S. Okasinski, X. Liu, Y. Liu, Q. Zeng, Z. Lu, *Nat. Commun.* **2017**, *8*, 15687.
[11] X. Zhao, S. Ning, W. Fu, S. J. Pennycook, K. P. Loh, *Adv. Mater.* **2018**, *30*, 1802397.
[12] W. O'reilly, *J. Magn. Magn. Mater.* **1994**, *137*, 167.
[13] D. J. Vaughan, J. A. Tossell, *Science* **1973**, *179*, 375.
[14] F. Wehland, U. Alt-Epping, S. Braun, E. Appel, *Phys. Earth Planet. Inter.* **2005**, *148*, 157.
[15] M. Gaspar, N. Grácio, R. Salgueiro, M. Costa, *Minerals* **2022**, *12*, 1248.
[16] R. Xin, J. Zhang, X. Sun, H. Li, Z. Ren, S. Yan, *Polymers* **2018**, *10*, 556.
[17] Y. Zheng, P. Pan, *Prog. Polym. Sci.* **2020**, *109*, 101291.
[18] J. E. Garcia, F. Rubio-Marcos, *J. Appl. Phys.* **2020**, *127*, 131102.
[19] S. H. Kang, K. Song, J. Jung, M. R. Jo, Y.-M. Kang, *J. Mater. Chem. A* **2014**, *2*, 19660.

[20] Y. Li, Z. G. Yu, L. Wang, Y. Weng, C. S. Tang, X. Yin, K. Han, H. Wu, X. Yu, L. M. Wong, D. Wan, X. R. Wang, J. Chai, Y.-W. Zhang, S. Wang, J. Wang, A. T. S. Wee, M. B. H. Breese, S. J. Pennycook, T. Venkatesan, S. Dong, J. M. Xue, J. Chen, *Nat. Commun.* **2019**, *10*, 3149.
[21] M.-J. Sun, Y. Liu, W. Zeng, Y. S. Zhao, Y.-W. Zhong, J. Yao, *J. Am. Chem. Soc.* **2019**, *141*, 6157.
[22] M. Ahart, M. Somayazulu, R. E. Cohen, P. Ganesh, P. Dera, H.-K. Mao, R. J. Hemley, Y. Ren, P. Liermann, Z. Wu, *Nature* **2008**, *451*, 545.
[23] B. Jaffe, R. S. Roth, S. Marzullo, *J. Appl. Phys.* **1954**, *25*, 809.
[24] R. Guo, L. E. Cross, S.-E. Park, B. Noheda, D. E. Cox, G. Shirane, *Phys. Rev. Lett.* **2000**, *84*, 5423.
[25] Y. Ding, Y. Qiu, K. Cai, Q. Yao, S. Chen, L. Chen, J. He, *Nat. Commun.* **2019**, *10*, 841.
[26] C. Fu, S. Bai, Y. Liu, Y. Tang, L. Chen, X. Zhao, T. Zhu, *Nat. Commun.* **2015**, *6*, 8144.
[27] S. Lin, W. Li, Z. Chen, J. Shen, B. Ge, Y. Pei, *Nat. Commun.* **2016**, *7*, 10287.
[28] P. Qiu, M. T. Agne, Y. Liu, Y. Zhu, H. Chen, T. Mao, J. Yang, W. Zhang, S. M. Haile, W. G. Zeier, J. Janek, C. Uher, X. Shi, L. Chen, G. J. Snyder, *Nat. Commun.* **2018**, *9*, 2910.
[29] G.-K. Ren, S. Wang, Z. Zhou, X. Li, J. Yang, W. Zhang, Y.-H. Lin, J. Yang, C.-W. Nan, *Nat. Commun.* **2019**, *10*, 2814.
[30] J. Zhang, L. Song, G. K. H. Madsen, K. F. F. Fischer, W. Zhang, X. Shi, B. B. Iversen, *Nat. Commun.* **2016**, *7*, 10892.
[31] H. Liu, X. Shi, F. Xu, L. Zhang, W. Zhang, L. Chen, Q. Li, C. Uher, T. Day, G. J. Snyder, *Nat. Mater.* **2012**, *11*, 422.
[32] P. Lukashev, W. R. L. Lambrecht, T. Kotani, M. Van Schilfgaarde, *Phys. Rev. B* **2007**, *76*, 195202.
[33] Z.-H. Ge, X. Liu, D. Feng, J. Lin, J. He, *Adv. Energy Mater.* **2016**, *6*, 1600607.
[34] Z.-H. Ge, L.-D. Zhao, D. Wu, X. Liu, B.-P. Zhang, J.-F. Li, J. He, *Mater. Today* **2016**, *19*, 227.
[35] N. Morimoto, G. Kullerud, *Am. Mineral.* **1963**, *48*, 110.
[36] K. Yamamoto, S. Kashida, *J. Solid State Chem.* **1991**, *93*, 202.
[37] S. Kashida, K. Yamamoto, *J. Phys.: Condens. Matters* **1991**, *3*, 6559.
[38] G. Will, E. Hinze, A. R. M. Abdelrahman, *Eur. J. Mineral.* **2002**, *14*, 591.
[39] L. Zhao, X. Wang, F. Y. Fei, J. Wang, Z. Cheng, S. Dou, J. Wang, G. J. Snyder, *J. Mater. Chem. A* **2015**, *3*, 9432.
[40] Y. Ding, *Am. Mineral.* **2005**, *90*, 1256.
[41] L. Pierce, P. R. Buseck, *Am. Mineral.* **1978**, *63*, 1.
[42] G. Donnay, J. D. H. Donnay, G. Kullerud, *Am. Mineral.* **1958**, *43*, 228.
[43] Z. Peng, S. Li, M. Weng, M. Zhang, C. Xin, Z. Du, J. Zheng, F. Pan, *J. Phys. Chem. C* **2017**, *121*, 23317.
[44] C. D. Flint, *Vibronic Processes in Inorganic Chemistry*, NATO ASI, Boston, UK **1989**.
[45] Wikibook, *Introduction to Inorganic Chemistry, LibreTexts*, Penn State University, USA **2023**, Ch. 5.8.
[46] Z.-H. Ge, Y.-X. Zhang, D. Song, X. Chong, P. Qin, F. Zheng, J. Feng, L.-D. Zhao, *J. Mater. Chem. A* **2018**, *6*, 14440.
[47] Z.-G. Li, S.-W. Gu, Y.-X. Zhang, T.-Y. Yang, R. Bao, J. Feng, Z.-H. Ge, *J. Alloys Compd.* **2023**, *953*, 169954.
[48] Y.-X. Zhang, T.-Y. Yang, Z.-Y. Wang, J. Feng, Z.-H. Ge, *Mater. Today Phys.* **2022**, *27*, 100808.
[49] J. Guo, J. Yang, Z.-H. Ge, B. Jiang, Y. Qiu, Y.-K. Zhu, X. Wang, J. Rong, X. Yu, J. Feng, J. He, *Adv. Funct. Mater.* **2021**, *31*, 2102838.
[50] J. Callaway, *Phys. Rev.* **1959**, *113*, 1046.
[51] J. Barthel, *Ultramicroscopy* **2018**, *193*, 1.